Interphase Forces of Lithium-Ion Battery Binders

Undergraduate Honors Research Thesis

Presented in partial fulfillment of the requirements for graduation “with Honors Research Distinction in Mechanical Engineering” in the undergraduate colleges of The Ohio State University

By

Michael Lee

Advisors:

Dr. Hanna Cho, Department of Mechanical and Aerospace Engineering

Dr. Jung-Hyun Kim, Department of Mechanical and Aerospace Engineering

Abstract

Future generations of battery materials with high energy densities will require the development and selection of new binders in order to maximize battery performance characteristics and lifespan. These binders will need favorable mechanical properties in order to maintain electrode integrity despite volume changes. In this study, the atomic force microscopy method of force spectroscopy is used to measure the mechanical properties of two industry standard binder materials, sodium alginate and polyvinylidene fluoride (PVdF) both in a dry state and immersed in di-methyl carbonate (DMC), a common electrolyte solvent. These samples are examined using a cantilever with a silicon tip in order to determine interphase forces characteristic of a silicon-based anode. Both materials experience significant reductions in adhesive force after immersion, but PVdF's adhesive force is reduced so far as to be unmeasurable using the current methodology. Both materials also experience a reduction in Young's modulus, although the elastic modulus of sodium alginate is significantly greater than that of PVdF both before and after immersion. These observations support previous research regarding the properties of these materials and their performance in battery cells and indicate that this methodology can be used for future measurements and comparisons of additional binders.

Acknowledgements

I offer my most sincere gratitude to both of my advisors. Dr. Hanna Cho is responsible for guiding me through the learning process regarding the technology, the theory, and the process that was necessary to complete this research, and her guidance has led me to accomplishments even beyond my involvement in her laboratory. Dr. Jung-Hyun Kim has offered me technical help and advice at every turn, and has done an incredible job helping to expand my understanding of topics beyond my immediate field of sight but relevant to my work. Without these two professors, none of my research or accomplishments would be possible.

I would also like to thank my previous lab partner, Rahul Reddi, for his teaching and guidance in my first year of work in the laboratory. Before his graduation, Rahul helped me with every aspect of laboratory work, and I am grateful for everything that his help has done for my own project.

Table of Contents

Table of Figures

Chapter 1: Background

1.1 Introduction to lithium-ion batteries

Changes and advancements in energy technology have strongly thrust battery technology into the forefront of research interest. From consumer electronics to fail proofing devices for national energy grids, and from the emerging luxury electric vehicles market to military UAVs, countless devices depend on battery technology to function. Several constraints govern the desirable performance parameters of these batteries. Favorable safety, capacity to be economically manufactured, and energy capacity with regards to both volume and weight are among the most significant of these parameters. For these reasons, lithium-ion batteries have emerged as the industry standard. The development of lithium-ion battery technology has revealed these cells to be capable of greater energy density than comparable technologies while maintaining reliability, safety, and rechargeability. The relatively attractive specific energy and specific power characteristics of these batteries can be noted in Figure 1. Lithium-ion batteries capable of retaining more than 400 W*h/kg have been implemented in a commercial setting.

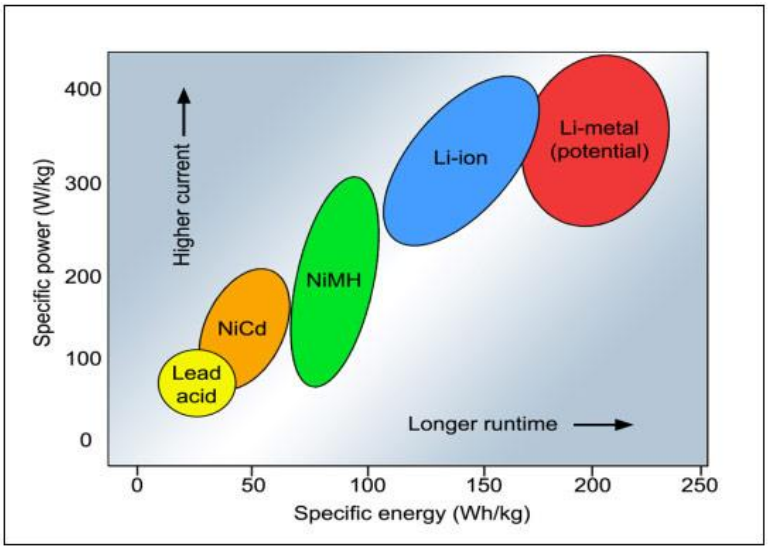

Figure 1: Battery energy density distribution by type ("The Global Battery Market")

1.2 Li-ion battery components

In order to understand the factors which influence the performance of these batteries, several components must be considered. A typical lithium-ion battery is primarily composed of three different materials. The cathode and anode materials exchange lithium ions and electrons in order to create a voltaic potential across the battery cell. These materials are connected by the electrolyte, typically a liquid, which is responsible for conducting the lithium ions between the two electrodes. A schematic of a lithium-ion battery cell including a layered, transition metal polyhedron-based cathode and a traditional graphite anode can be found in Figure 2. Each one of these materials offers unique contributions to battery functionality, and thus unique opportunities to improve or change the performance characteristics of the battery.

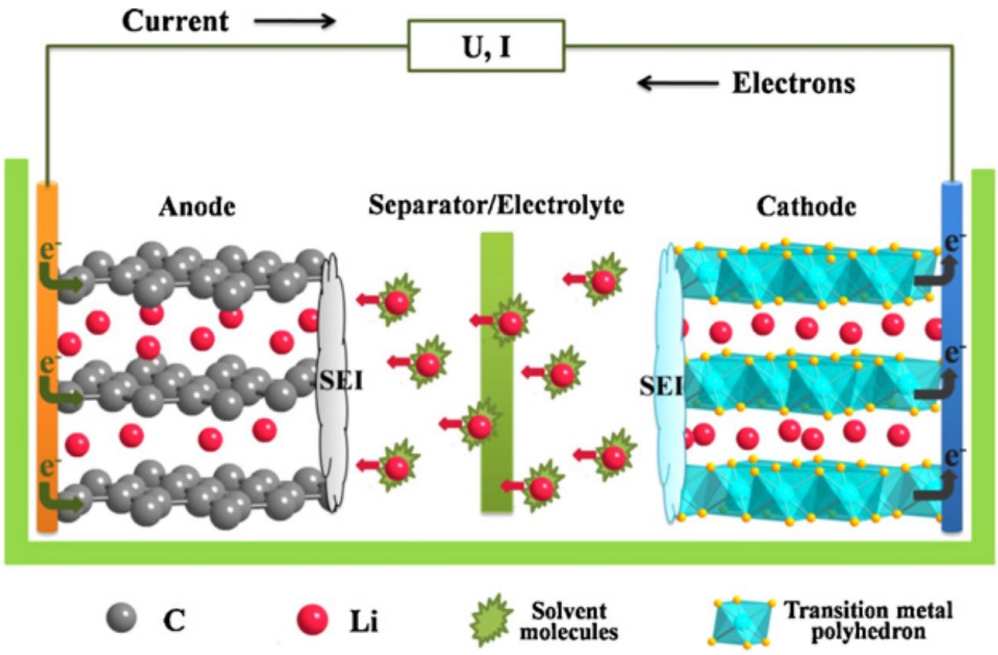

Figure 2: Li-ion battery internal schematic (Xu et al.)

First, careful electrolyte selection is a key factor in battery performance. Optimization of ionic conductivity characteristics is extremely important for enabling favorable current capacity.

In addition, during the first battery cycle, liquid electrolyte causes the formation of a region known as the Solid-Electrolyte Interface (SEI) between the liquid electrolyte and the solid electrode material. According to the research of Verma et al., an SEI which demonstrates relatively high ionic conductivity and low electrical conductivity is capable of providing optimal battery performance, and significant research exists regarding this phenomenon. Many proprietary electrolyte mixtures have been developed for use in commercial applications.

Next, the electrode materials contribute greatly to battery performance. Both the cathode, or positive electrode, and anode, or negative electrode, have the potential for engineering improvements in order to improve battery characteristics. Each electrode is comprised of a mixture of three materials: the active material, a carbon powder, and a binder, as seen in Figure 3. A mixture of these three materials is immersed in electrolyte and connected to the current collector, and each of these materials has a significant impact on battery characteristics.

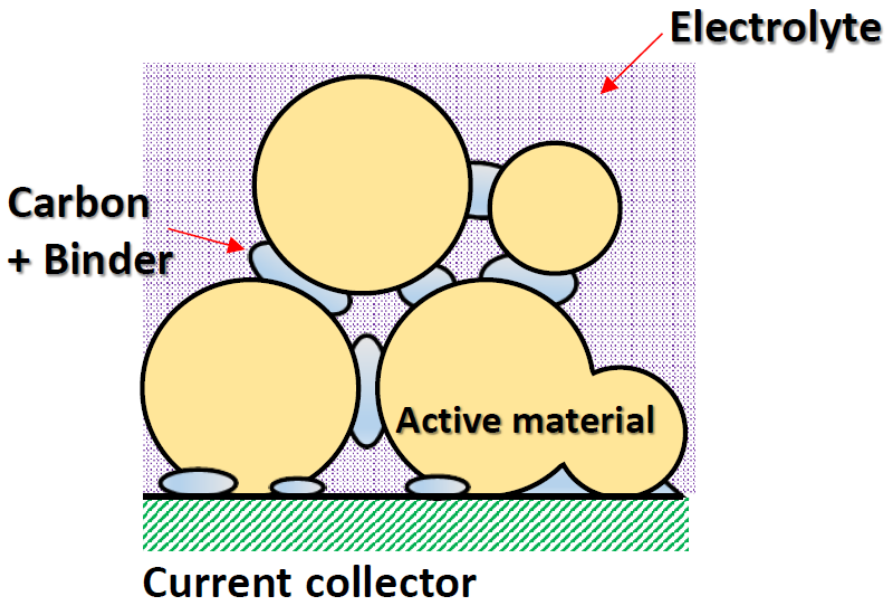

Figure 3: Electrode components

First, the active material, which is reduced or oxidized during the charge/discharge cycle, is a key component. Voltaic potential, ionic conductivity, and the ratio of active material necessary

to house lithium ions are all very important factors. Many researchers principally investigate new and experimental cathode active materials using unique three-dimensional structures and novel chemical formulations. Xu et al. investigate the effect of active material morphology on performance for many of these experimental materials. In addition, although graphite is widely used as a standard anode material, considerable research has been conducted regarding the use of silicon as an alternative, as it can hold much more lithium per weight and volume than graphite. The next electrode material is carbon, which is universally used in lithium-ion battery electrodes. Carbon in the form of a nanoscale particulate is added to electrode material mixtures in order to retain maximum electrical conductivity between the full electrode material and the current collector. The final component of the electrode material is the binder. Typically a polymer, the binder is responsible for maintaining the structural integrity of the electrode material, physically holding it together and preventing structural failure. Both electrical and ionic conductivity must be contained throughout the electrode material for consistent battery functionality. The importance of this interaction between carbon and binder is examined in detail by Fransson et al.

1.3 Failure of Li-ion batteries

Despite many favorable performance characteristics, lithium-ion battery technology is not without significant flaws. Macroscopic failure of a lithium-ion battery cell is likely to have catastrophic consequences, including ignition. At the microscopic scale, fast charge or discharge rates can lead to phenomena such as lithium plating, or even dendrite formation, which is capable of rendering a battery cell nonfunctional or even shorting it. The factors that lead to these failures and the results thereof are widely studied, and one detailed examination was completed by Bieker et al. However, such failures can largely be mitigated through careful design of charge protocols, fabrication procedures, and enclosures in order to prevent situations capable of leading to catastrophic failure.

The much more universal means of failure of lithium-ion batteries is degradation due to repeated cycling. This degradation causes major reductions in battery current capacity over the course of hundreds of battery cycles, and eventually causes the battery to cease functioning entirely. Analysis has revealed that the root cause of this degradation is microstructural failure of the electrode material. During the battery cycle, the cathode and anode material must exchange lithium ions. The lithiation process causes major volume increases in most active materials, causing them to repeatedly swell up to 250% of their initial volume before returning to their original state over the charge/discharge cycle. This behavior and the degradation it causes have been studied by Chen et al. While this phenomenon is not extreme in the traditional carbon anode material, it is a major issue with the silicon anode, as examined by Ko et al., and many cathode materials. Repeated volume changes cause stress on the structure of the electrode material, eventually resulting in the formation of microscale cracks. This phenomenon is most significant near the battery's current collector. Cracking in the electrode material reduces the overall electrical conductivity of the material, eventually resulting in reduced current capacity and battery death. The most significant volume changes are present in materials with high energy capacities, making a way to mitigate this cracking failure necessary to propel the development of high-energy lithium-ion batteries with long lifespans.

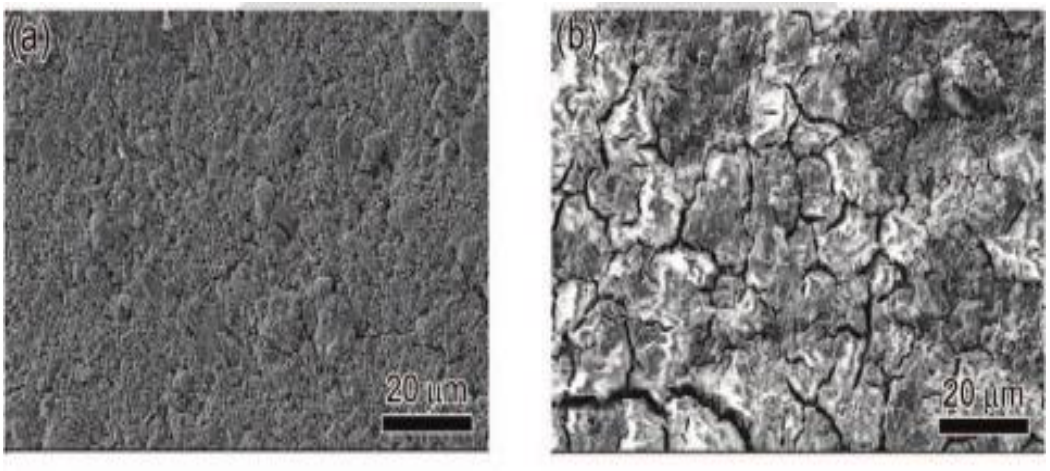

Figure 4: Cathode cracking at a) electrode center and b) electrode end (Chen et al.)

1.4 Typical Li-ion binders

The largest contributor to the mechanical integrity of the electrode material is the binder. Binder selection has a significant effect on specific capacity and capacity changes of the battery. The interaction of the binder with the electrolyte is also an important factor in binder selection. Polyvinylidene fluoride (PVdF) has become established as an industry standard binder in lithium-ion batteries due to manufacturing cost and performance characteristics. However, several proposed alternatives offer considerable performance increases through adaptation of alternative binders, including styrene-butadiene rubber (SBR), lithium polyacrylate (LiPAA), and sodium alginate. Initial research regarding these materials has proved them to be capable of favorable performance when fabricated into a full battery cell and subjected to charge/discharge cycle testing. Koo et al. and Pieczonka et al. write at length about the favorable attributes of these materials. In order to make informed selections regarding future binder materials, it is important to gain a fundamental understanding of the characteristics which impact these binders' performance.

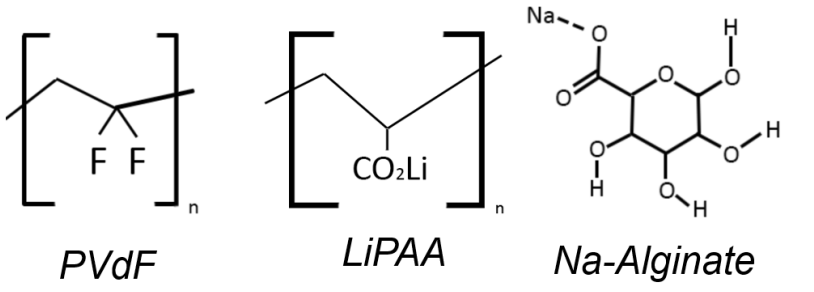

Figure 5: Chemical structure of PVdF, LiPAA, and sodium alginate binders

Two fundamental mechanical properties are important to consider when addressing the binder's integrity. Adhesion between the binder and other electrode materials is important because adhesive forces are responsible for holding components together and preventing delamination. Elasticity is also important, as it correlates with the binder's resistance to stresses caused by the active material's volume changes. While these properties are well-understood and

easily tested at the macroscale through such methods as peel and stress/strain testing, two unique factors impact binder performance in battery applications. The first is the scale. The critical mechanical failure which causes battery degradation occurs at the microscale, and thus a complete understanding of the mechanical properties exhibited by binder materials at the microscale, rather than the macroscale, is necessary. While micro- and macro- scale material properties are related, current knowledge is not sufficient to directly predict one from the other. The other major factor is the presence of electrolyte within the battery cell. Electrolyte significantly weakens interphase forces and influences the elasticity of the immersed material, and testing a material immersed in electrolyte via traditional methods is not a simple task. A new method must be established in order to gain key insight into the performance of binder materials at the appropriate scale, and in-situ.

1.5 Statement of purpose

The purpose of this study is to establish a method capable of consistently and accurately measuring the physical properties of binders for lithium-ion batteries. This method must be able to measure these properties at the microscale, and must be able to measure these properties both in a dry state and when immersed in electrolyte. With these requirements in mind, atomic force microscopy is posited as an appropriate technology for this study.

1.6 Atomic force microscopy

Atomic force microscopy (AFM) is a microscopy method capable of high-resolution and extremely precise imaging and contact measurements. In order to collect this data, AFM employs a cantilever with a nanoscale tip, which is used to probe the surface of a sample. A laser is reflected off of the surface of the cantilever and onto an array of photodiodes. Once calibrated, the voltage output of these photodiodes can be used to precisely measure the deflection of the cantilever. A schematic of this setup can be found in Figure 6. Once the calibration process is complete, the

sample can be examined using a variety of methods. Basic imaging using the AFM is accomplished by one of two methods. In the first method, known as contact imaging, the cantilever is lightly touched to the surface, and then moved along it. Any changes to the deflection of the cantilever are used to measure the local height of the sample surface and control the cantilever height. In the second method, known as tapping mode imaging, the cantilever is vibrated at a resonant frequency and then touched to the sample surface. In this mode, not only can the sample height be precisely measured, but the phase shift between the input and deflection signals can be mapped and used to determine the relative energy absorption of different areas of the sample. Significantly, AFM methods, including those which involve cantilever vibration, are completely possible with a sample immersed in liquid. This fundamental advantage over more traditional microscopy techniques makes AFM a favorable technology for the examination of battery materials in-situ.

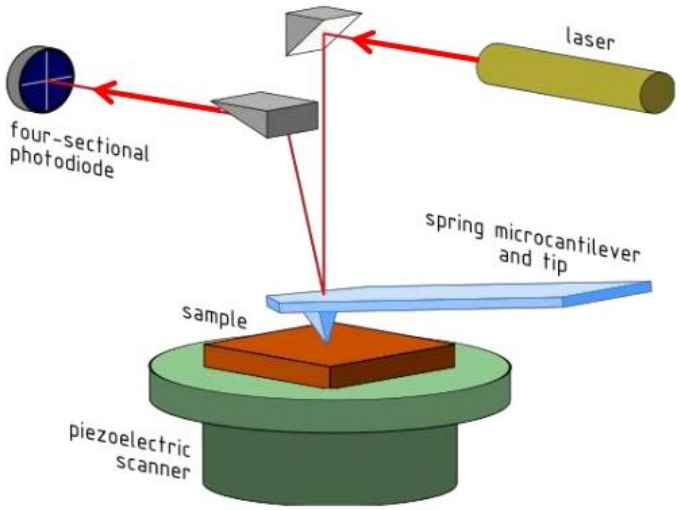

Figure 6: Atomic force microscopy diagram (Bhattacharjee)

1.7 Force spectroscopy

In addition to imaging methods, AFM offers another technique which is essential to examination of microscale physical properties of samples. This technique is known as force spectroscopy.

During force spectroscopy, the AFM's cantilever is lowered onto the surface of the sample. The cantilever tip is pressed into the surface of the sample with a set force. Then, the cantilever is retracted from the sample until the tip detaches from the sample. The deflection of the cantilever is precisely recorded during both the extension and retraction phases and can be visualized as a force curve, as seen in Figure 7. The resulting force data can be analyzed in order to make significant conclusions regarding the mechanical properties of the sample. During the retraction phase, for example, any adhesive force between the cantilever tip and sample will be seen as a negative deflection value. Multiplying this negative deflection peak by the known spring constant of the cantilever will reveal the total adhesive force between these components. The contact region of the force curve will also reveal key data. The slope of the relationship between deflection and cantilever height in this region will positively correlate with elastic modulus. By modelling contact mechanics in this region, it is possible to predict the elastic modulus of the sample based on this data.

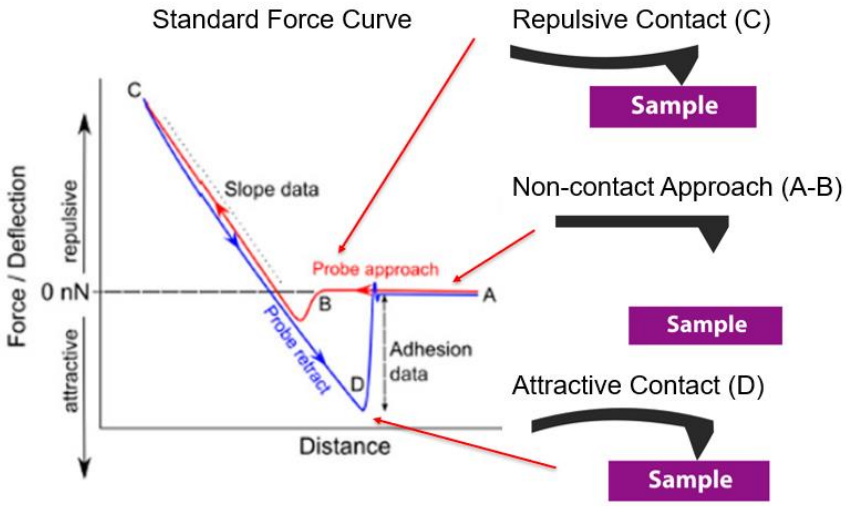

Figure 7: Basic force spectroscopy curve ("Home")

Several proposed contact mechanics models are capable of appropriately predicting the relationship between indentation and sample elasticity for data gathered via force spectroscopy. The cantilever tip used in the force spectroscopy method can be modelled as a ball with a known

radius and mechanical properties attached to a spring of a known stiffness. The first and simplest contact model is the Hertz model, which relates indentation distance to applied force in a nonlinear fashion based on tip and sample elastic modulus. Next, the JKR model offers a revised version of the Hertz model which accounts for adhesion forces between the indenter and the sample surface. Other advanced contact mechanics models include the DMT and Oliver-Pharr models, which account for noncontact forces and imbalances between deformation of the surface and tip.

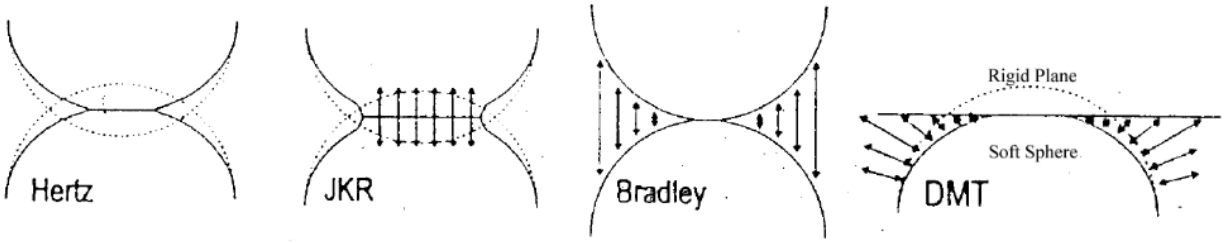

Figure 8: Visualization of assorted contact mechanics models (Johnson)

For the purpose of this experiment, the Hertz contact mechanics model was deemed both computationally flexible and widely documented enough to provide a thorough computational foundation for determining the Young's modulus of the sample. Via the Hertzian model, the relationship between the force exerted on the sample's surface and the indentation of a sphere-shaped protrusion into the sample's surface can be expressed in the following equations 1 and 2. A visualization of the Herzian contact mechanics model can be found in Figure 9.

Equation 1: Hertz model indentation

$$u = \left(\frac{2F^2}{{E_*}^2}\right)^{1/3}$$

Equation 2: Hertz model relative elastic modulus formulation

$$\frac{1}{E_*} = \frac{1}{2}\left(\frac{1-{v_1}^2}{E_1} + \frac{1-{v_2}^2}{E_2}\right)$$

Where

$u =$ indentation distance

$F =$ total force

$v_1 =$ cantilever Poisson's ratio

$v_2 =$ sample Poisson's ratio

$E_1 =$ cantilever Young's modulus

$E_2 =$ sample Young's modulus

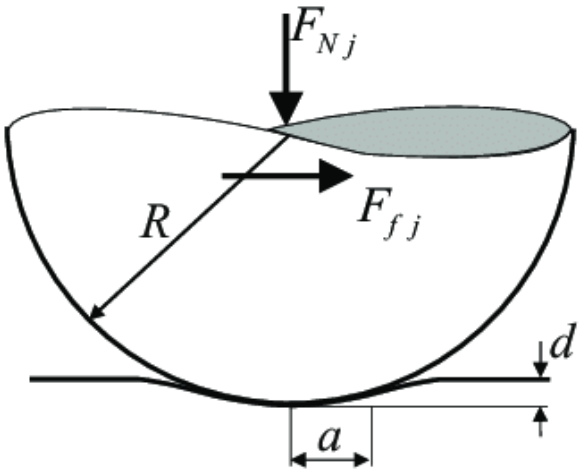

Figure 9: Hertz indentation model (Nguyen et al.)

Chapter 2: Experimental Methodology

2.1 Sample fabrication

Two batches of samples were prepared. An PVdF solution was created by mixing 5% HSV900 PVdF by mass into a N-methyl 2-pryyolidone solution. Similarly, a sodium alginate solution was created by mixing 3% sodium alginate by mass with deionized water. Both solutions were cast onto a stainless steel substrate, and then dried in an oven at 50 degrees Celsius for one hour. The samples were then moved into a vacuum oven and dried at 80 degrees Celsius for around 12 hours before being moved for examination.

2.2 Force spectroscopy method

In order to complete examination of each sample, each sample was placed in the Asylum Research Fluid Cell Lite shown in Figure 11. A large scratch was made into the surface of each sample and cleaned appropriately. This region of exposed substrate was used to complete calibration of an AC160 cantilever, as seen in Figure 10, which has a spring constant of around 40 N/m. This cantilever was selected based on the force requirements of nanoindentation in a sample with a Young's modulus in the 100 MPa to 50 GPa range. A 20-by-20 micrometer area of the surface of each sample was selected, and a 16-by-16 point force map of this area was taken. Then, dimethyl carbonate (DMC) electrolyte was added to the sample, completely covering the surface. The optical laser sensitivity was recalibrated using the exposed substrate area and holding the spring constant of the cantilever constant. Finally, another 20-by-20 micrometer area of the sample was selected, and another 16-by 16 force map was collected. Additional force maps were collected in this area each 30 minutes for the next seven hours, with adjustments to the cantilever height, imaging area, and level of DMC made as necessary.

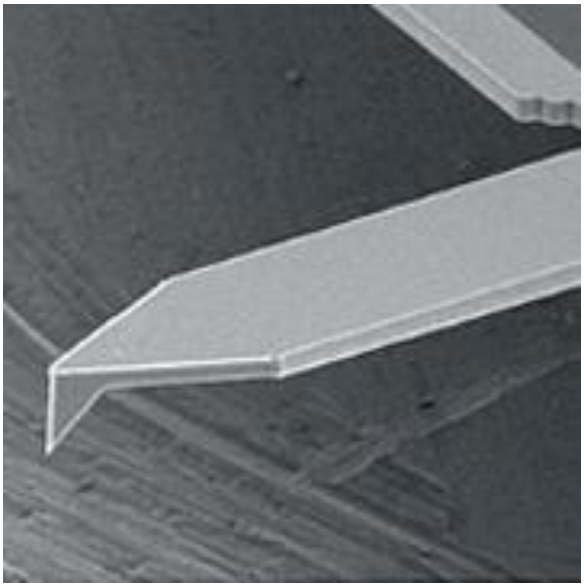

Figure 10: AC160 cantilever SEM image ("OMCL-AC160TS")

Figure 11: Asylum research fluid cell lite ("Fluid Cell Lite")

2.3 Data analysis

The resulting force data for each sample was analyzed. The negative deflection peak of each retraction force curve was identified, and the maximum adhesion force was calculated by multiplying the magnitude of this deflection by the known spring constant. Then, a contact mechanics model was selected to calculate the elastic modulus at each point. For force curves without an appreciable adhesive region, the Hertz method was selected, while the JKR method was selected for regions with an adhesive region. A model fit was used to calculate the elastic modulus at each point for each measurement on each sample.

Once an adhesion force and an elastic modulus value were calculated at each point on the sample, the full set of values of each mechanical property at each point and for each sample was graphed into a histogram format. Then, a Gaussian distribution was applied to each histogram in order to identify the characteristics of a single characteristic data peak. The mean value and standard deviation of each data set was recorded.

Chapter 3: Results and Discussion

3.1 PVdF

Both dry state data and seven hours of in-situ force spectroscopy data were collected for each sample. The dry state, 0.5, and 7 hour measurements were selected in order to demonstrate the geometry and general trends in force data. Characteristic force curves were selected at each time and can be seen in Figure 12. Notably, a significant reduction in adhesive force occurs when electrolyte is added to the sample. For the PVdF sample, the adhesive forces demonstrated after immersion proved too minute to be measured with the selected cantilever. Several contributing factors may affect this behavior. Polymers in a dry state may exhibit residual moisture forces which are not present in a wet state. In the case of PVdF, significant forces such as dipole interactions and hydrogen bonding are not possible due to the polymer's structure. The van der Waals forces which are exhibited between the PVdF sample and the Si tip in such an environment may not be strong enough to create a measurable negative deflection in the selected cantilever. Selection of a cantilever with a smaller spring constant may enable the measurement of these adhesive forces, but at the expense of adequate indentation for nanoindentation modelling. The slope of the indentation-force relationship decreased with immersion time, and the consequences of this reduction on calculated elastic modulus can be noted in the following figures.

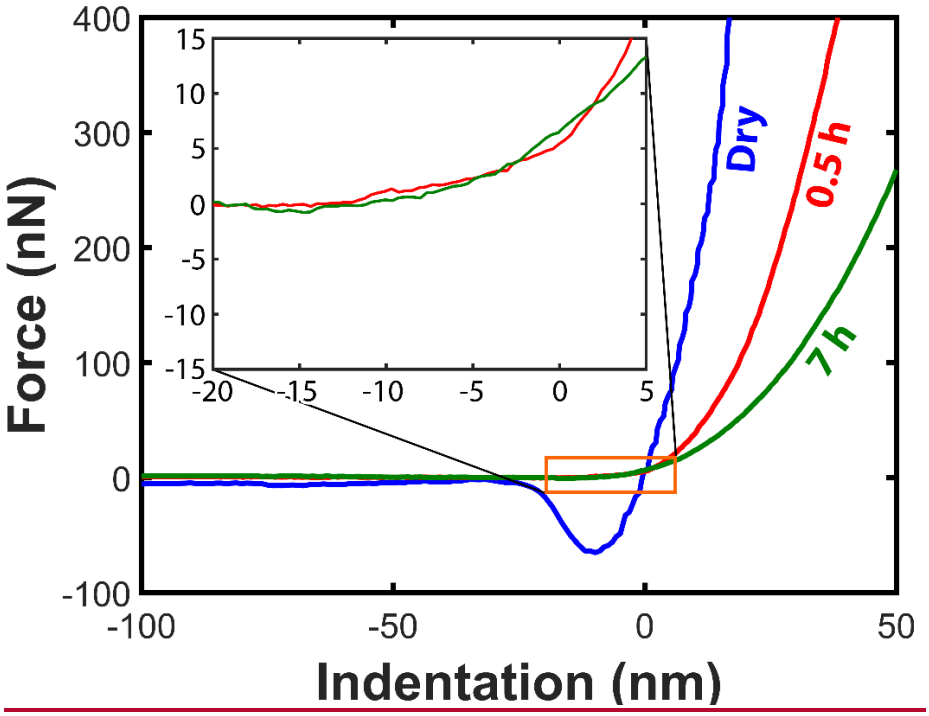

Figure 12: Selected PVdF force data

As seen in Figure 13, PVdF showed a major reduction in Young's modulus upon addition of electrolyte. The initial dry state Young's modulus of PVdF was measured to be around 868 MPa. This value shows significant deviation from literature value established by Kim et al. via nanoindentation methods. This group fabricated samples using spin coating of a polymeric film 5 micrometers in thickness, and their examination revealed PVdF to exhibit a Young's modulus of 6.4 GPa. Possible explanations for this discrepancy include fabrication methodology and structural differences exhibited by the film and casting methods. However, this discrepancy must be further examined to increase confidence in this method. After immersion, the Young's modulus of the sample decreased to 308.5 MPa and marginally decreased for two hours of immersion, until settling at around 261.3 MPa. A steady-state behavior is present at this time. It should be noted that despite a heterogeneous morphology, surface geometry was not determined to significantly influence measurements. The global trend in Young's modulus demonstated by this sample can be seen in Figure 14.

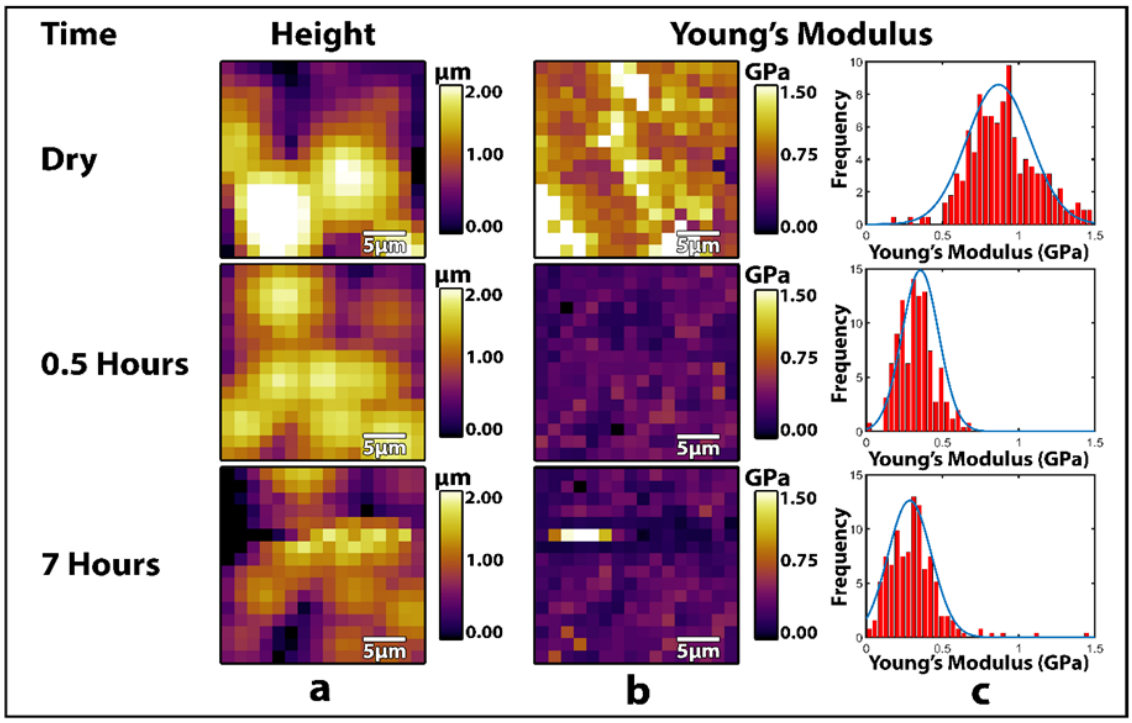

Figure 13: Visualization of PVdF a) height map b) Young's modulus map c) Young's modulus histogram

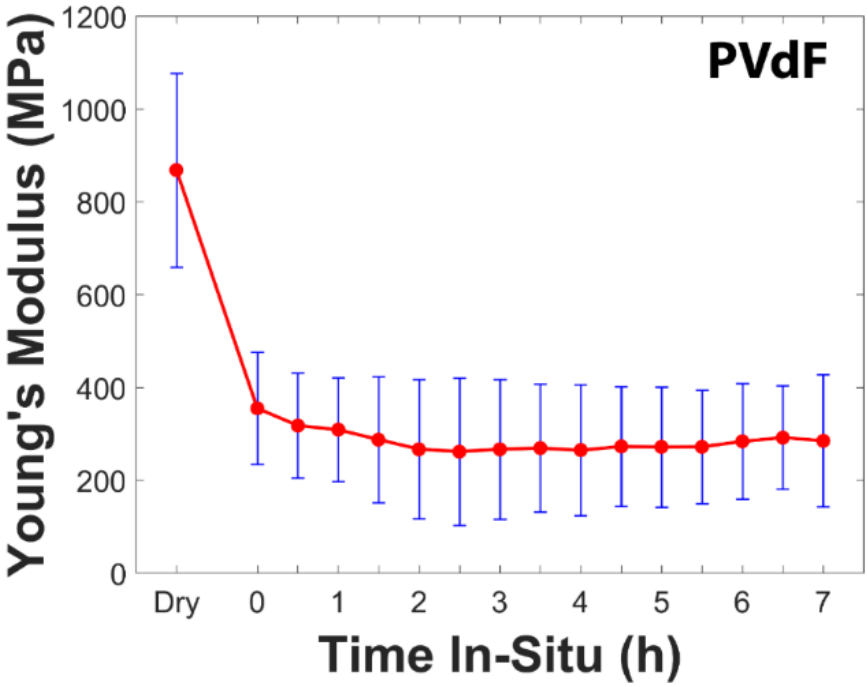

Figure 14: PVdF Young's modulus trend

3.2 Sodium alginate

In contrast to PVdF, sodium alginate showed a lesser reduction in adhesion when immersed in electrolyte. The adhesive forces of this sample after immersion were measurable, meaning that they were found to be at least an order of magnitude greater than those demonstrated by PVdF in the in-situ environment. The sodium alginate sample also experienced a lesser change in the force-indentation slope over time. However, it should be noted that the nonlinear nature of the Herzian contact model causes greater effects on the calculated Young's Modulus the greater the slope of the force/indentation curve. Individual characteristic force curves for this sample can be seen in Figure 15.

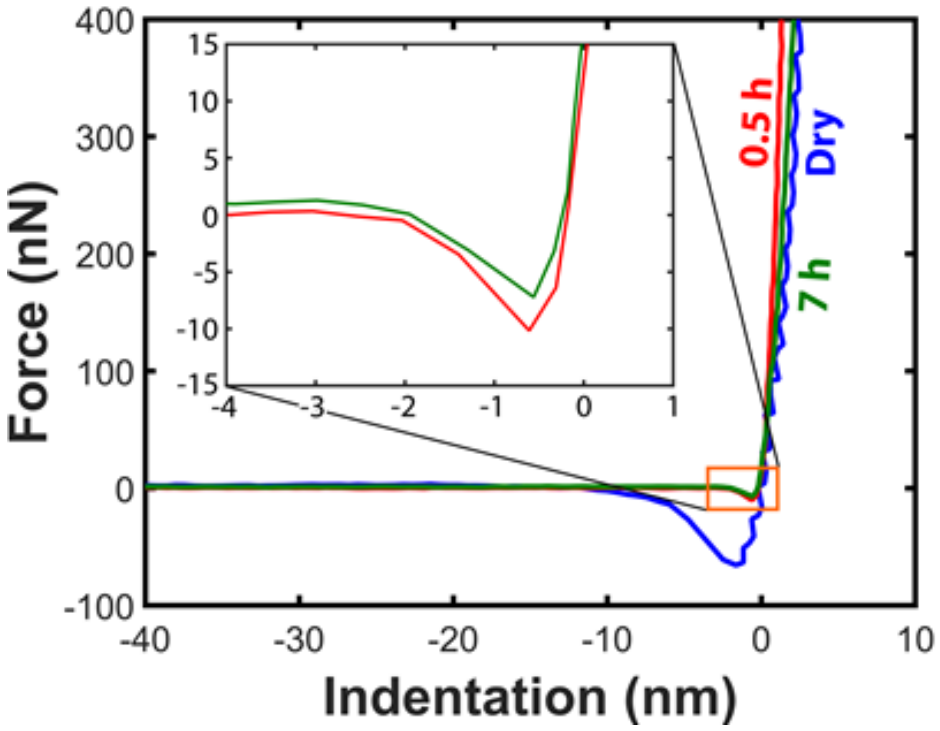

Figure 15: Selected sodium alginate force data

Sodium alginate's dry state behavior resulted in an abnormal elastic modulus distribution. Selected maps to demonstrate the distribution of the Young's modulus values can be seen in

Figure 16. Significant geometric effects on the calculated Young's modulus were noted in the dry state measurement, and a region of force data influenced by sample slope was neglected. A one-degree of freedom flattening mask was applied to height data for this sample in order to properly allow visualization of surface characteristics. An initial dry state elasticity of around 33.39 GPa reduced to 14.17 GPa after an hour of immersion. Initial measurements after immersion of the sodium alginate sample resulted in an unusually broad distribution of values. Notably, the stiffness of the sodium alginate sample both before and after immersion was found to be significantly greater than that of the PVdF sample. The trend of sodium alginate's in-situ Young's modulus can be found in Figure 17.

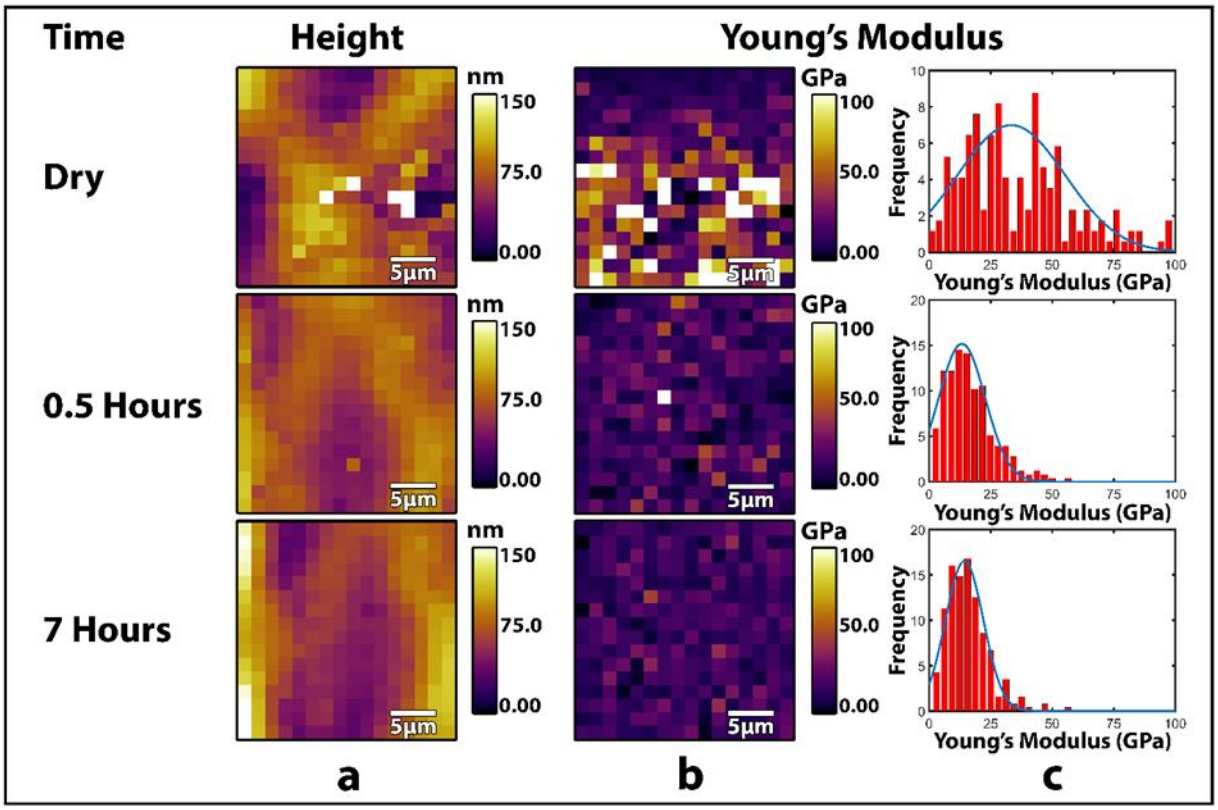

Figure 16: Visualization of sodium alginate a) height map b) Young's modulus map c) Young's modulus histogram

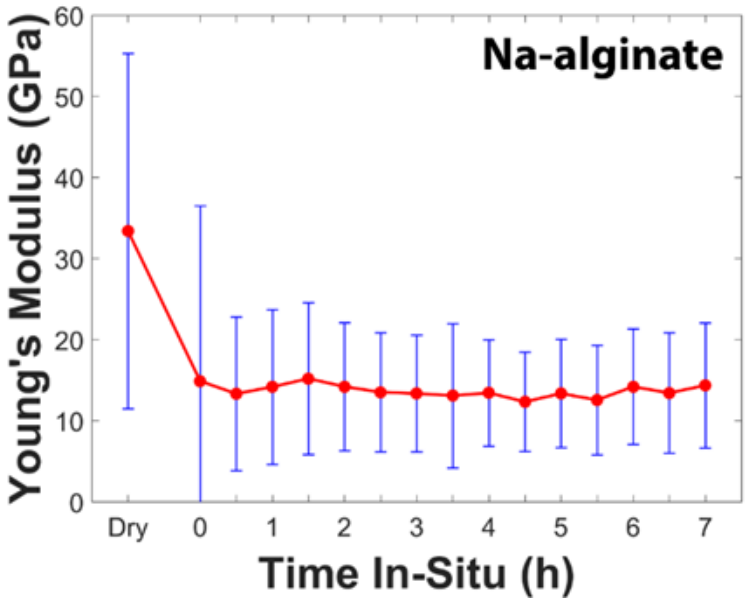

Figure 17: Sodium alginate Young's modulus trend

Despite similar dry state adhesion values, the addition of electrolyte influenced a measurable difference between the adhesive forces demonstrated by the binder samples. Unlike PVdF, the adhesive forces demonstrated by the sodium alginate sample while immersed in electrolyte were found to be measurable. The maps of these values can be found in Figure 18. The complete trend of the adhesive force exhibited by sodium alginate can be found in Figure 19. Research by Ryou et al. and Kovalenko et al. indicates that the structure of sodium alginate allow formation of hydrogen bonds between the sodium alginate and surface oxidation of silicon. Combined with dipole forces which are not present for PVdF, this explanation may account for the difference in the order of magnitude of forces observed between these two binders and the silicon probe. Complete force map sets for each type of data can be found in Appendix A.

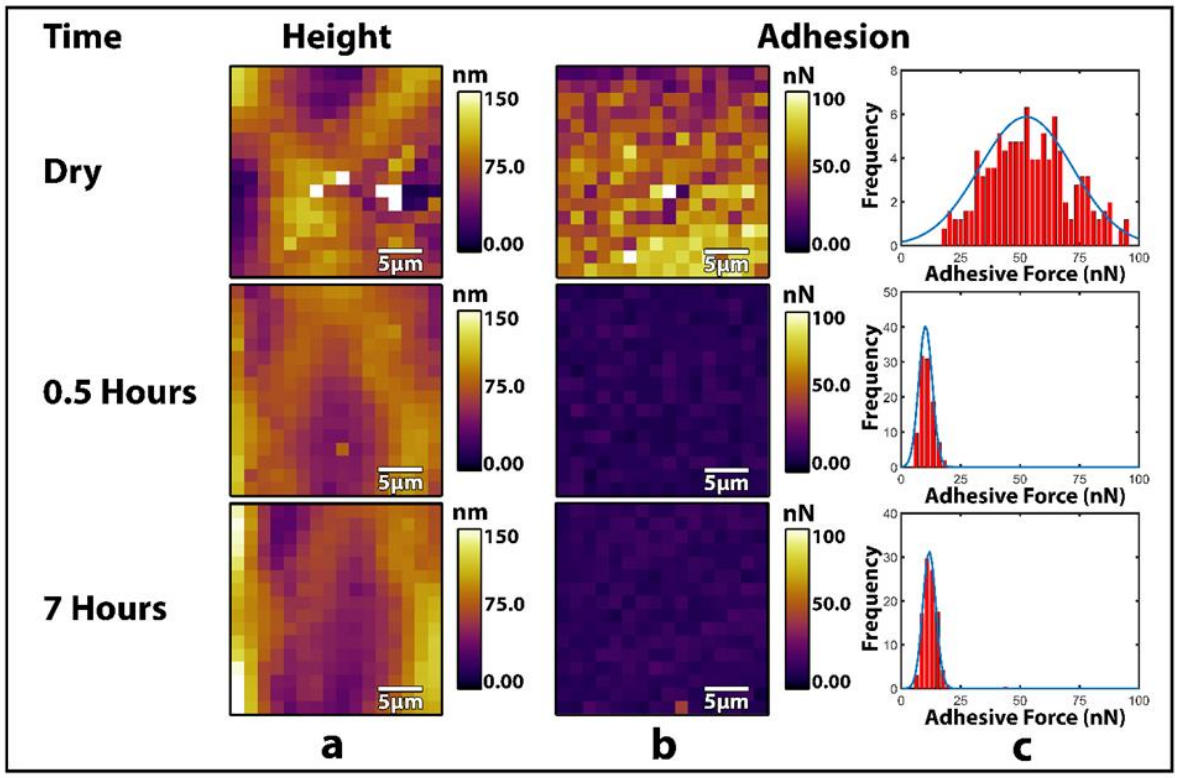

Figure 18: Visualization of sodium alginate a) height map b) adhesion map c) adhesion histogram

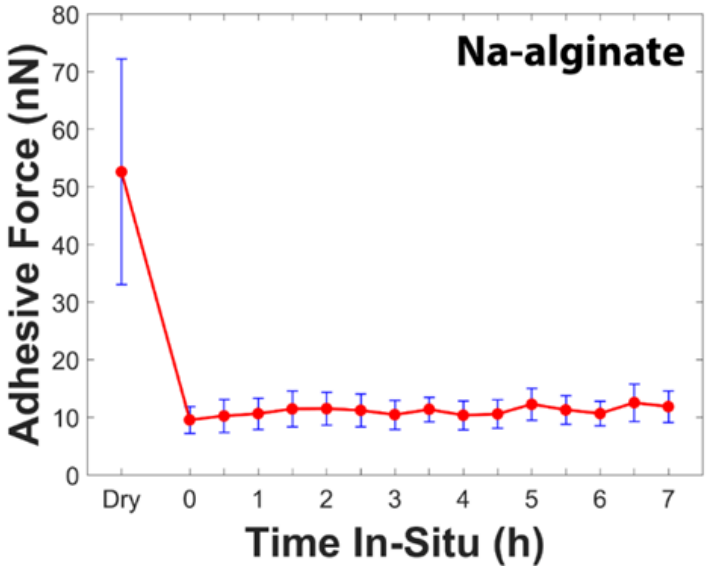

Figure 19: Sodium alginate adhesion trend

Chapter 4: Conclusion

The experimental methodology outlined in this study proved capable of consistently measuring physical property data relevant to the performance characteristics of common lithium ion battery binders. The Young's moduli of both sodium alginate and PVdF samples were measured and directly compared. This data, provided with an account of the fabrication method of the samples, is a valuable addition to the literature on these materials. The adhesive forces demonstrated between sodium alginate and Si were also found, and it was shown that PVdF's adhesive forces are significantly less. These measurements and comparisons support previous research regarding the performance characteristics of these binders in operation, and from these comparisons, it can be concluded that the use of high-stiffness materials which are capable of dipole and hydrogen bonding can improve the performance characteristics and prolong the degradation of lithium ion batteries.

Future work will aid in furthering the interpretation of these findings. First, the analysis of additional binder samples using the same methodology will allow further comparisons to be made, and provide context for the distinction between the effects of adhesive forces and binder stiffness on battery performance. Second, the introduction of a second cantilever with a reduced stiffness of less than 0.1 N/m would enable a resolution several hundred times greater than the current setup with which to measure adhesive forces. This method would have to be used in supplement to the current methodology, as such a cantilever would not be capable of adequate indentation for contact mechanics modelling. Finally, a means of fabrication of a cantilever with a particle of another material fixed by epoxy or other method to the tip would enable measurements of adhesive forces between additional relevant pairs of battery materials. Together, these three avenues of study can provide a comprehensive characterization of lithium-ion battery interphase forces and enable future development of materials for favorable battery characteristics.

Bibliography

Bhattacharjee, Joy. “Atomic Force Microscope: Fundamental Principles.” *LinkedIn SlideShare*, 11 Nov. 2015, www.slideshare.net/joybiitk/atomic-force-microscope-fundamental-principles.

Bieker, Georg, et al. “Electrochemical in Situ Investigations of SEI and Dendrite Formation on the Lithium Metal Anode.” *Physical Chemistry Chemical Physics*, vol. 17, no. 14, 2015, pp. 8670–8679., doi:10.1039/c4cp05865h.

Chen, Jianchao, et al. “Unveiling the Roles of Binder in the Mechanical Integrity of Electrodes for Lithium-Ion Batteries.” *Journal of The Electrochemical Society*, vol. 160, no. 9, 2013, doi:10.1149/2.088309jes.

“Fluid Cell Lite for MFP-3D Atomic Force Microscopes | Asylum Research - Asylum Research.” *Oxford Instruments*, afm.oxinst.com/products/mfp-3d-liquid-environmental-control/mfp-3d-fluid-cell-lite.

Fransson, L. “Influence of Carbon Black and Binder on Li-Ion Batteries.” *Fuel and Energy Abstracts*, vol. 43, no. 4, 2002, p. 262., doi:10.1016/s0140-6701(02)86297-x.

“Home.” *High-Quality Atomic Force Microscopes for a Lower Price - AFM Workshop*, www.afmworkshop.com/afm-products/modes/afm-advanced-force-distance-curves.

Jee, Taekwon, et al. “Effect of Microstructures of PVDF on Surface Adhesive Forces.” *Tribology Letters*, vol. 26, no. 2, 2006, pp. 125–130., doi:10.1007/s11249-006-9163-z.

Johnson, Kenneth L. *Contact Mechanics*. Cambridge Univ. Press, 2004.

Kim, Jung Sub, et al. “Effect of Polyimide Binder on Electrochemical Characteristics of Surface-Modified Silicon Anode for Lithium Ion Batteries.” *Journal of Power Sources*, vol. 244, 2013, pp. 521–526., doi:10.1016/j.jpowsour.2013.02.049.

Ko, Minseong, et al. “Challenges in Accommodating Volume Change of Si Anodes for Li-Ion Batteries.” *ChemElectroChem*, vol. 2, no. 11, 2015, pp. 1645–1651., doi:10.1002/celc.201500254.

Koo, Bonjae, et al. “A Highly Cross-Linked Polymeric Binder for High-Performance Silicon Negative Electrodes in Lithium Ion Batteries.” *Angewandte Chemie*, vol. 124, no. 35, 2012, pp. 8892–8897., doi:10.1002/ange.201201568.

Kovalenko, I., et al. “A Major Constituent of Brown Algae for Use in High-Capacity Li-Ion Batteries.” *Science*, vol. 334, no. 6052, 2011, pp. 75–79., doi:10.1126/science.1209150.

Nguyen, Xuan-Ha, et al. “Improvements of Piezo-Actuated Stick–Slip Micro-Drives: Modeling and Driving Waveform.” *Coatings*, vol. 8, no. 2, 2018, p. 62., doi:10.3390/coatings8020062.

“OMCL-AC160TS.” *Olympus Micro Cantilevers : OMCL-AC160TS*, probe.olympus-global.com/en/product/omcl_ac160ts_r3/spec.html.

Pieczonka, Nicholas P. W., et al. “Lithium Polyacrylate (LiPAA) as an Advanced Binder and a Passivating Agent for High-Voltage Li-Ion Batteries.” *Advanced Energy Materials*, vol. 5, no. 23, 2015, p. 1501008., doi:10.1002/aenm.201501008.

Pieczonka, Nicholas P. W., et al. “Lithium Polyacrylate (LiPAA) as an Advanced Binder and a Passivating Agent for High-Voltage Li-Ion Batteries.” *Advanced Energy Materials*, vol. 5, no. 23, 2015, p. 1501008., doi:10.1002/aenm.201501008.

Ryou, Myung-Hyun, et al. “Lithium-Ion Batteries: Mussel-Inspired Adhesive Binders for High-Performance Silicon Nanoparticle Anodes in Lithium-Ion Batteries (Adv. Mater. 11/2013).” *Advanced Materials*, vol. 25, no. 11, 2013, pp. 1570–1570., doi:10.1002/adma.201370074.

Siqueira, D.freitas, et al. “Adhesion and Morphology of PVDF/PMMA and Compatibilized PVDF/PS Interfaces.” *Polymer*, vol. 32, no. 6, 1991, pp. 990–998., doi:10.1016/0032-3861(91)90584-6.

"The Global Battery Market – an Industry Report Review." *News about Energy Storage, Batteries, Climate Change and the Environment*, 2 Aug. 2014, www.upsbatterycenter.com/blog/global-battery-market-industry-report-review/.

Verma, Pallavi, et al. "A Review of the Features and Analyses of the Solid Electrolyte Interphase in Li-Ion Batteries." *Electrochimica Acta*, vol. 55, no. 22, 2010, pp. 6332–6341., doi:10.1016/j.electacta.2010.05.072.

Xu, Bo, et al. "ChemInform Abstract: Recent Progress in Cathode Materials Research for Advanced Lithium Ion Batteries." *ChemInform*, vol. 44, no. 12, 2013, doi:10.1002/chin.201312211.

Appendix A: Supplemental Figures

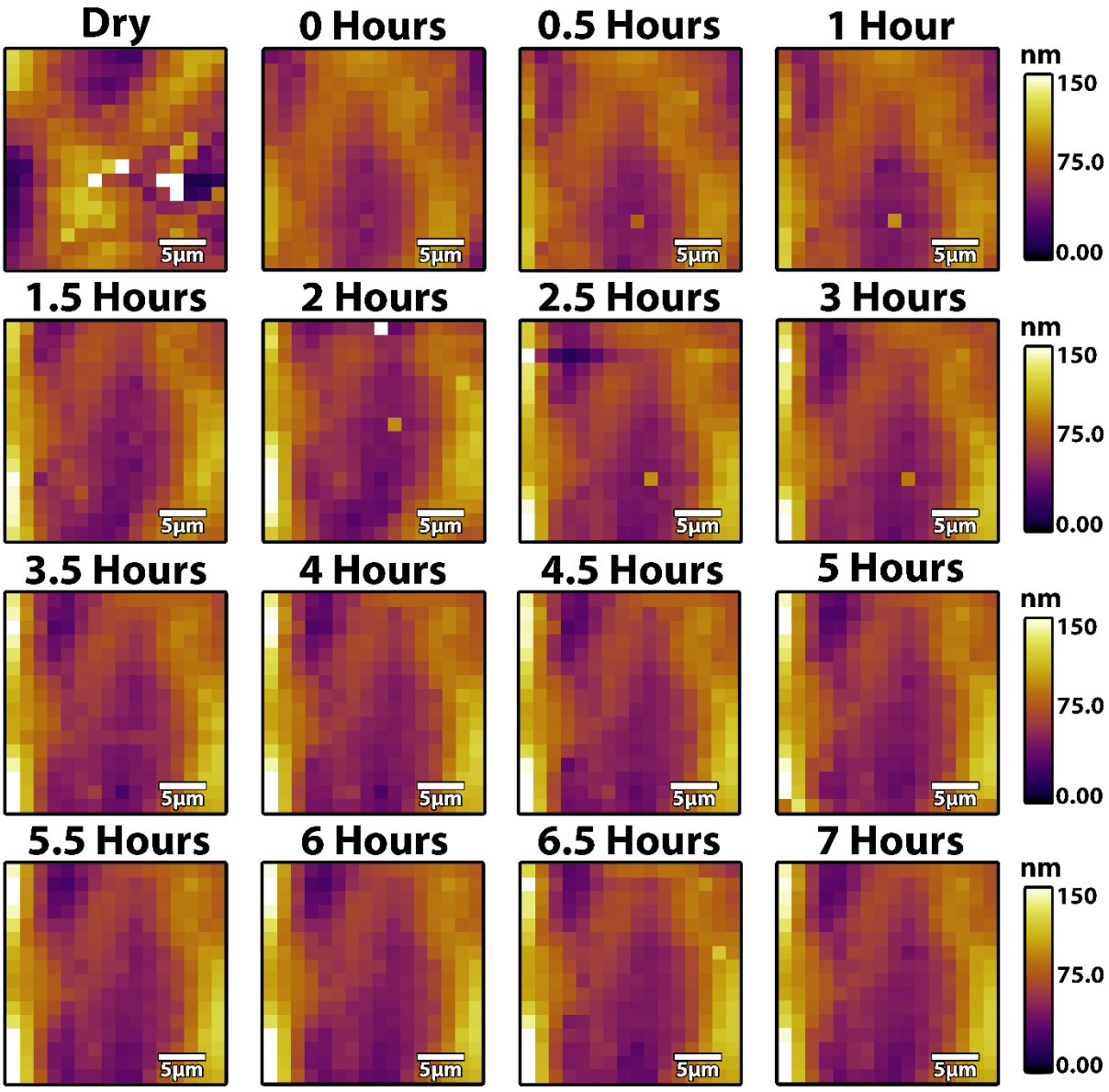

Figure A1. AFM force spectroscopy height maps for Na-alginate. A one-degree flattening filter has been applied to account for the surface slope.

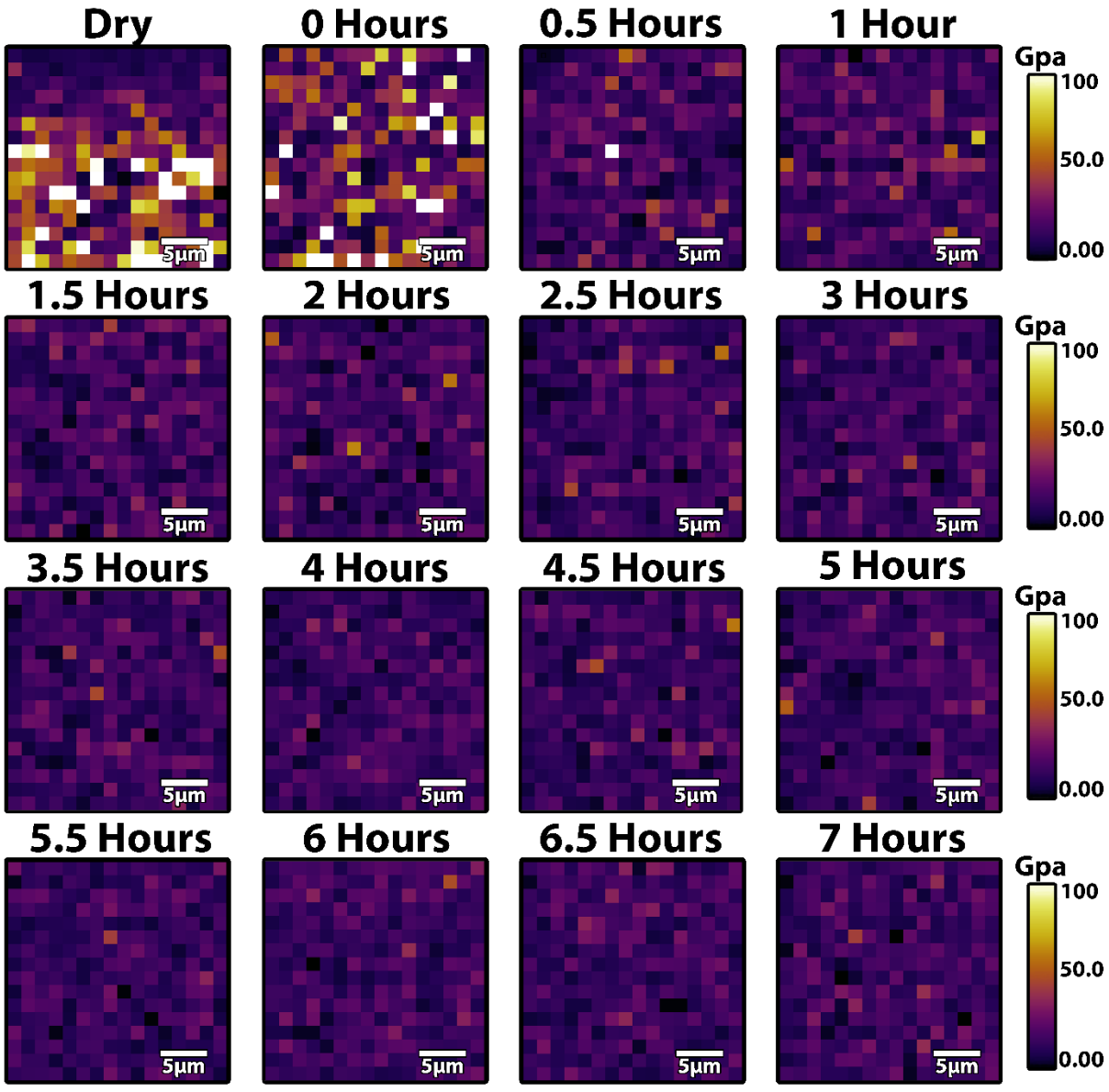

Figure A2. AFM force spectroscopy Young's modulus maps for Na-alginate. In order to account for geometric irregularities, the first five rows of the dry state map are excluded from statistical analysis.

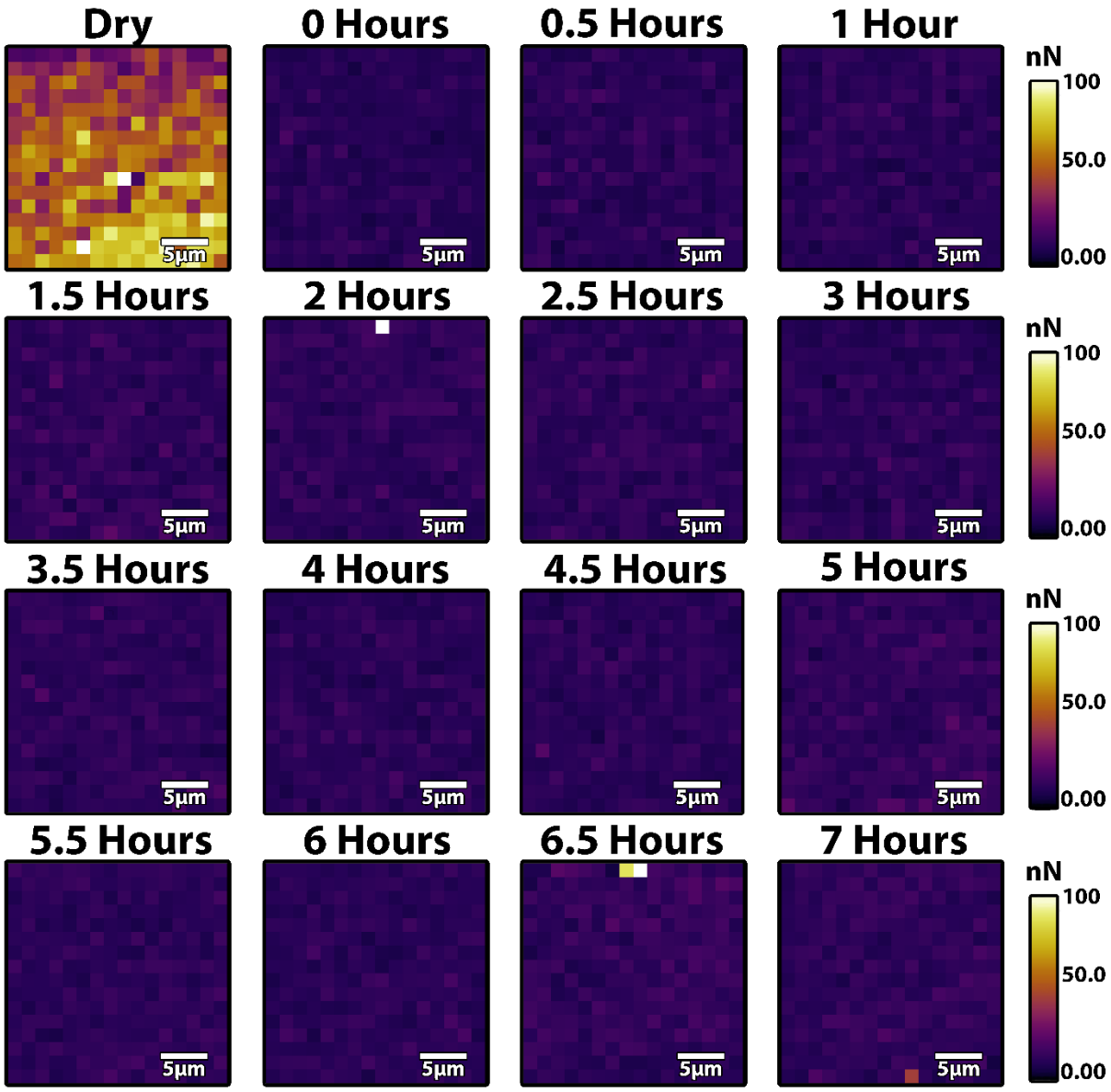

Figure A3. AFM force spectroscopy adhesive force maps for Na-alginate.

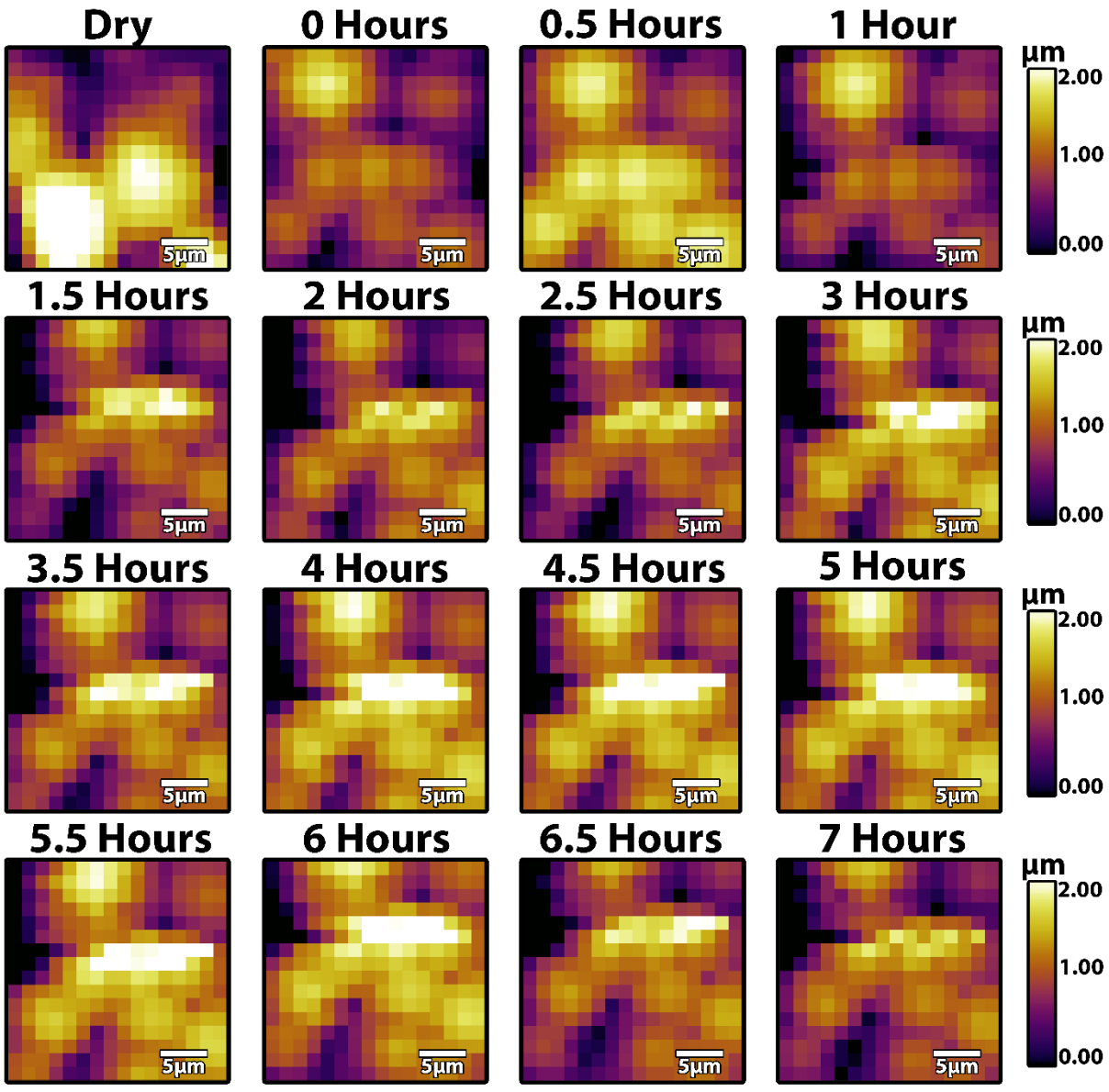

Figure A4. AFM force spectroscopy height maps for PVdF.

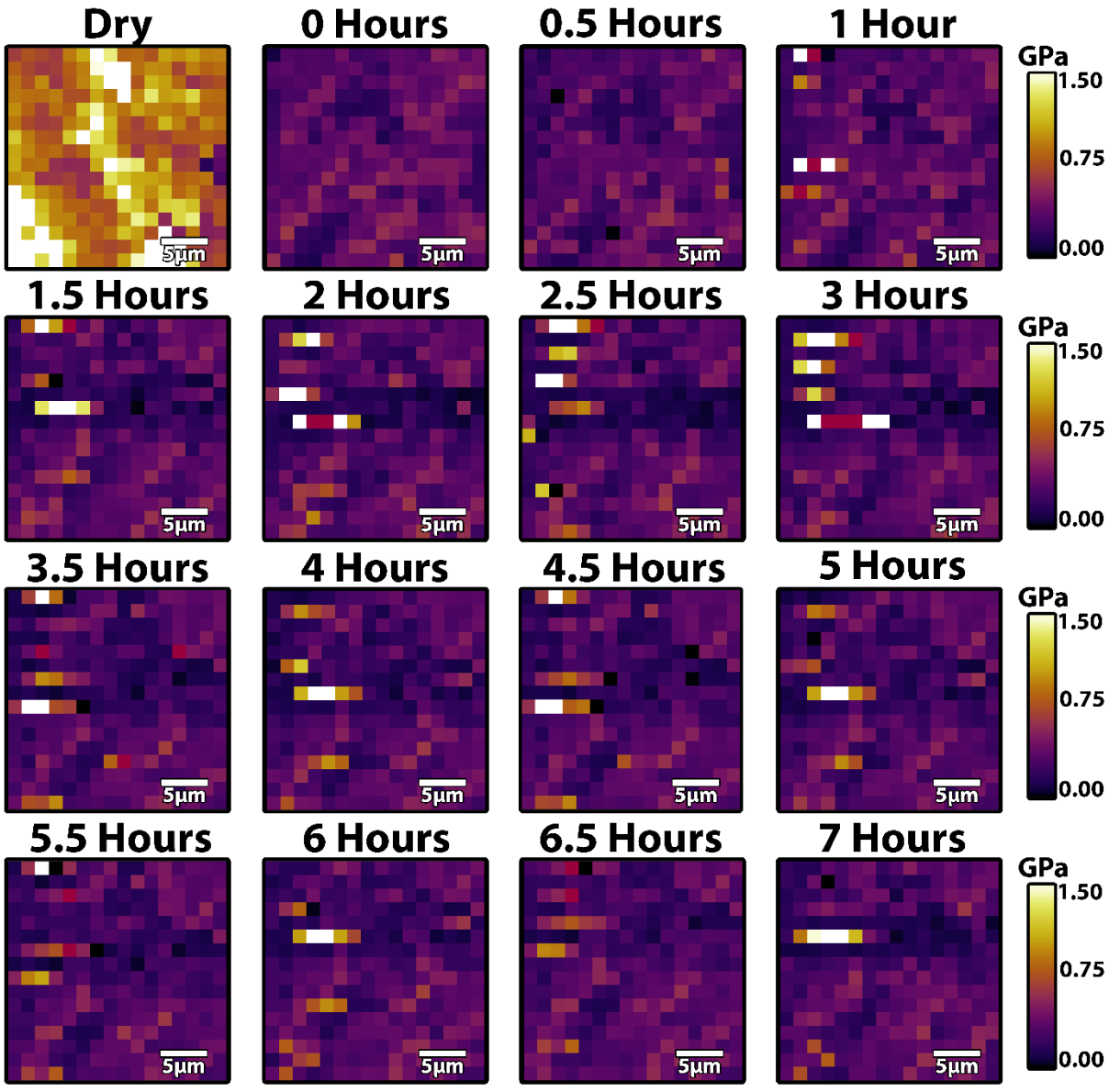

Figure A5. AFM force spectroscopy Young's modulus maps for PVdF.